Adatom and Nanoparticle Dynamics on Single-Atom Catalyst Substrates

Matteo Farnesi Camellone, Filip Dvořák, Mykhailo Vorokhta, Andrii Tovt, Ivan Khalakhan, Viktor Johánek, Tomáš Skála, Iva Matolínová, Stefano Fabris, Josef Mysliveček

Abstract

Single-atom catalysts represent an essential and ever-growing family of heterogeneous catalysts. Recent studies indicate that besides the valuable catalytic properties provided by single-atom active sites, the presence of single-atom sites on the catalyst substrates may significantly influence the population of supported metal nanoparticles coexisting with metal single atoms. Treatment of ceria-based single-atom catalysts in oxidizing or reducing atmospheres was proven to provide a precise experimental control of the size of supported Pt nanoparticles and, correspondingly, a control of catalyst activity and stability. Based on dedicated surface science experiments, ab initio calculations, and kinetic Monte Carlo simulations, we demonstrate that the morphology of Pt nanoparticle population on ceria surface is a result of a competition for Pt atoms between Pt single-atom sites and Pt nanoparticles. In an oxidizing atmosphere, Pt single-atom sites provide strong bonding to single Pt atoms and Pt nanoparticles shrink. In reducing atmosphere, Pt single-atom sites are depopulated and Pt nanoparticles grow. We formulate a generic model of Pt redispersion and coarsening on ceria substrates. Our model provides a unified atomic-level explanation for a variety of metal nanoparticle dynamic processes observed in single-atom catalysts under stationary or alternating oxidizing/reducing atmospheres and allows us to classify the conditions under which nanoparticle ensembles on single-atom catalyst substrates can be stabilized against Ostwald ripening.

Introduction

Activity, selectivity, and stability of most heterogeneous catalysts depend sensitively on the size of supported metal nanoparticles. (1,2) Experimental techniques and practical approaches have been developed, targeting the nanoparticle size during catalyst activation, (3,4) operation, (5,6) and regeneration, (7,8) with the aim to optimize the catalyst utilization and to improve understanding of nanoparticle dynamic changes throughout the catalyst lifetime. With the realization of single-atom catalysts, the range of controlled metal nanoparticle sizes has reached a limit of one supported metal atom. (9,10) Single supported metal atoms do not represent

a thermodynamically stable entity on their own. To prevent nucleation of metal atoms to metal nanoparticles, single-atom catalyst substrates must be available, providing sites with strong enough chemical bonding to single metal atoms to overcome metal cohesion. (11,12) Still, the stabilization of single metal atoms on the catalyst substrate does not guarantee a single-atom catalyst operation. Often, the strong bonding of single atoms to the substrate compromises their catalytic activity (13−15) or single atoms are destabilized by interaction with reactants during catalyst operation and metal nanoparticles become the active phase instead. (16,17)

The highly dynamic behavior of metal load on a single-atom catalyst substrate has been documented for platinum (Pt) on ceria (CeO_2). Ceria can provide strong bonding to metal nanoparticles resulting in high metal dispersion and small nanoparticle size. (18) Recently, it was proven that Pt nanoparticles on ceria/alumina substrates are destabilized in oxidizing conditions and at high temperatures and decompose to Pt single atoms bonded to O atoms at surface defects on ceria, particularly at monoatomic surface steps. (19) Such Pt single atoms show small activity toward CO oxidation. (20,21) Activation of Pt single atoms on ceria for low-temperature CO oxidation can be achieved via treatment of the single-atom catalyst under reducing conditions when, in turn, Pt single atom traps are destabilized and three-dimensional Pt nanoparticles of an optimal size nucleate. (22,23) When Pt nanoparticles further grow in size by Ostwald ripening and low-temperature CO oxidation activity is suppressed, catalyst treatment under an oxidizing atmosphere can reset the Pt single-atom dispersion and make the catalyst ready for a new activation. (22) These results indicate exciting possibilities for activation, regeneration, and long-time operation of metal nanoparticle catalysts supported on single-atom catalyst substrates (24−27) and call for elucidating the mechanisms of Pt redispersion and coarsening on ceria under oxidizing and reducing atmospheres.

We address the issues of Pt redispersion and coarsening in a model system of Pt nanoparticles on CeO_2(111) single crystalline substrate. (28) Flat CeO_2(111) surfaces can be investigated by microscopic and spectroscopic techniques of surface science, obtaining direct quantitative information unavailable for real Pt−ceria catalysts: density of surface defects or single-atom sites, (29) charge state of the surface, (30) and occupation of single-atom sites by single Pt atoms. (31) Previously, such quantitative information, combined with ab initio calculations, allowed identifying Pt single-atom dispersion on CeO_2(111) at monoatomic steps acting as single-atom traps. (31) Configuration of the stable single Pt atom was identified as Pt^{2+} ion bonded to four neighboring surface O atoms in a square-planar configuration. (31) Capacity of monoatomic steps on CeO_2(111) was determined as one Pt^{2+} single ion per one step Ce site. (31) Binding energy of Pt at the single-atom sites was investigated as a function of the concentration of Pt and O atoms at CeO_2(111) step edges. (32) In the presence of excess O atoms at step edges (in vacuum or in oxidizing atmosphere), Pt atoms are accommodated at step edges as single Pt^{2+} ions with binding energy E_1^{ox} larger than Pt cohesive energy E_c. In the absence of excess or lattice O atoms at step edges (in vacuum or in reducing atmosphere), single Pt atoms are accommodated at step edges as partially charged $Pt^{\delta+}$ species with binding energy E_1^{re} smaller than Pt cohesive energy E_c.

In the present work, we perform dedicated surface science experiments revealing the dynamic character of Pt load on CeO_2(111), particularly the thermally activated nature of the redispersion of deposited Pt to single Pt^{2+} ions, (19,31−33) and Pt coarsening and redispersion in alternating reducing and oxidizing conditions. (22,23,34) With further support from ab initio calculations we formulate a generic model of Pt redispersion and coarsening comprising Pt adatom diffusion on CeO_2(111) terraces, Pt adatom interaction with single-atom traps at CeO_2(111) step edges, and Pt adatom interaction with Pt nanoparticles on CeO_2(111) surface. We show that thermal activation during Pt redispersion and coarsening is required for breaking Pt–Pt bonds in Pt nanoparticles on the way toward minimization of the total energy of the Pt/CeO_2(111) system. Under oxidizing conditions, a capture of Pt adatoms in single-atom traps is preferred ($E_1^{ox} > E_c$) and Pt nanoparticles shrink. Under reducing conditions, single-atom traps are depopulated ($E_1^{re} < E_c$) and Pt nanoparticles grow by Ostwald ripening. Kinetic Monte Carlo simulations within the proposed model allow us to identify general conditions under which metal nanoparticle catalysts on single-atom catalyst substrates can be optimized and operated in a stable, sinter-resistant manner.

Results

Thermally Activated Nature of Pt Redispersion on CeO_2(111)

To achieve an efficient redispersion of Pt deposit to supported Pt single atoms on model and real CeO_2 substrates, thermal activation is required. (19,31−33) We investigate this process in detail in a series of surface science ultra-high vacuum (UHV) experiments in which Pt is deposited at 300 K on CeO_2(111) samples prepared with well-defined concentrations of surface monoatomic steps, providing single-atom Pt adsorption sites. (19,27,31,32) Upon Pt deposition, the samples are subjected to repeated flash annealing at gradually increasing temperatures and characterized with synchrotron radiation photoelectron spectroscopy (SRPES). In the SRPES of Pt 4f, the Pt^{2+} signal corresponds to the amount of occupied Pt single-atom sites, whereas the Pt^0 signal represents partially charged $Pt^{\delta+}$ atoms and Pt nucleated as metal nanoparticles (Figure S1a,e,i). (31−33) The fraction of Pt^{2+} signal in the total Pt 4f signal thus allows us to determine the fraction of Pt deposit dispersed as single atoms. No Pt^{4+} signal is observed by SRPES in the present experiments.

We repeat these experiments on four CeO_2(111) samples prepared with step densities 6, 11, 15, and 16% monolayer (ML), always depositing 7% ML Pt. 1 ML represents the density of Ce atoms on the CeO_2(111) surface (7.9×10^{14} cm^{-2} or 7.9 nm^{-2}). The results are summarized in Figure 1. For each sample, a progressive redispersion of Pt is observed with increasing temperature. Three other effects can be identified. At 300 K, the fraction of Pt deposit dispersed as single atoms is increasing with increasing step concentration. Upon final annealing at 700 K, the fraction of Pt deposit dispersed as single atoms adopts two values. For the samples where the step density is higher than the amount of deposited Pt, the majority of Pt is dispersed as single atoms. For the sample where the step density is lower than the amount of deposited Pt, redispersion of Pt is incomplete. Finally, for the samples showing almost complete redispersion, an accelerated transient to the redispersed

state becomes apparent between 550 and 650 K, indicating a presence of an energy barrier to redispersion.

Figure 1

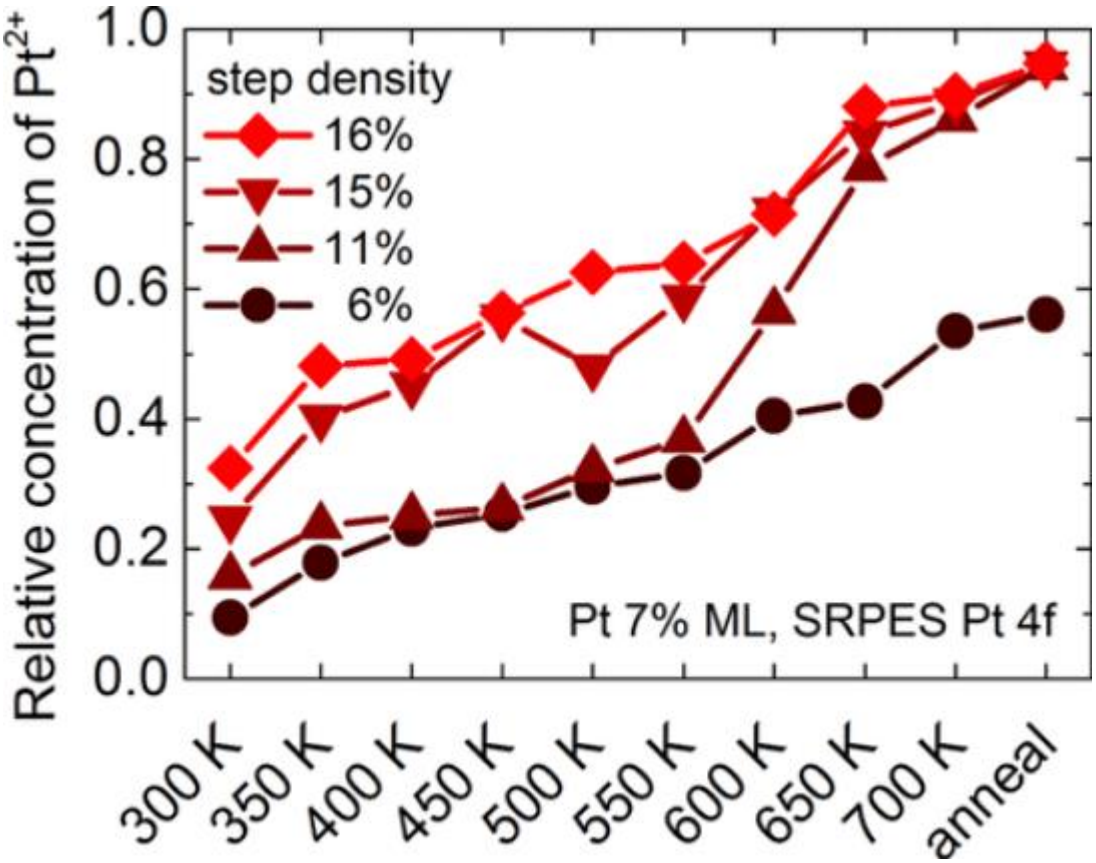

Figure 1. Redispersion of Pt deposited on CeO_2(111) in UHV. Pt was deposited at 300 K and flash-annealed in UHV to gradually increasing temperatures. The final step of the thermal treatment is annealing in UHV at 700 K for 5 min.

Redispersion and Coarsening of Pt Load on CeO_2(111) in Oxidizing and Reducing Conditions

Redispersion of Pt load on ceria nanoparticles under oxidizing conditions and subsequent coarsening under reducing conditions have been documented previously by means of transmission electron microscopy (TEM). (19,22,35) Here, we perform analogous experiments on model CeO_2(111) surfaces by means of SRPES and scanning tunneling microscopy (STM). On the CeO_2(111) surface with 15% ML of monoatomic steps, we deposit Pt at 300 K and anneal at 700 K in UHV to obtain Pt redispersion. Afterward, we perform alternating cycles of sample reduction (in 1×10^{-5} Pa CH_3OH) and sample oxidation (in 1×10^{-5} Pa O_2, see Experimental Procedures). In between the cycles, we characterize the chemical state of the sample by SRPES. We chose CH_3OH as a reducing agent because, in contrast to CO or H_2, it strongly interacts with clean CeO_2(111) surfaces and provides a reliable reduction of the CeO_2(111) surface under UHV conditions of surface science

experiments. (36) Reduction with CH_3OH does not change the density of monoatomic steps on CeO_2(111) surfaces. (32)

We repeat these experiments on four CeO_2(111) samples prepared with Pt amounts of 2, 6, 16, and 26% ML (0.2–2.1 Pt atoms/nm^2, cf. ref (27)). The results are summarized in Figure 2a. On all samples, we observe coarsening of the Pt deposit (decrease of the Pt^{2+} signal, increase of the Pt^0 signal) upon reduction treatments ("red1"–"red5") and redispersion (increase of the Pt^{2+} signal, decrease of the Pt^0 signal) upon oxidation treatments ("ox1"–"ox5"). Coarsening and redispersion also influence the total Pt 4f signal due to partial screening of the Pt^0 signal from metallic Pt nanoparticles. Screening is becoming more efficient for larger nanoparticles; the total Pt 4f signal can thus serve as a qualitative indication of the Pt nanoparticle size. For Pt amounts smaller than the step density (2 and 6% ML Pt), redispersion on the as-prepared samples ("Pt as prep") is almost complete, and subsequent coarsening and redispersion of Pt in the five observed reduction/oxidation cycles is very reversible. For Pt amounts larger than the step density (16 and 26% ML Pt), redispersion on the as-prepared samples is incomplete. Subsequent coarsening and redispersion cycles exhibit a progressive extinction of the Pt^{2+} signal accompanied by a decrease of the total Pt 4f signal, indicating an overall growth of metallic Pt nanoparticles at the expense of atomically dispersed Pt.

Figure 2

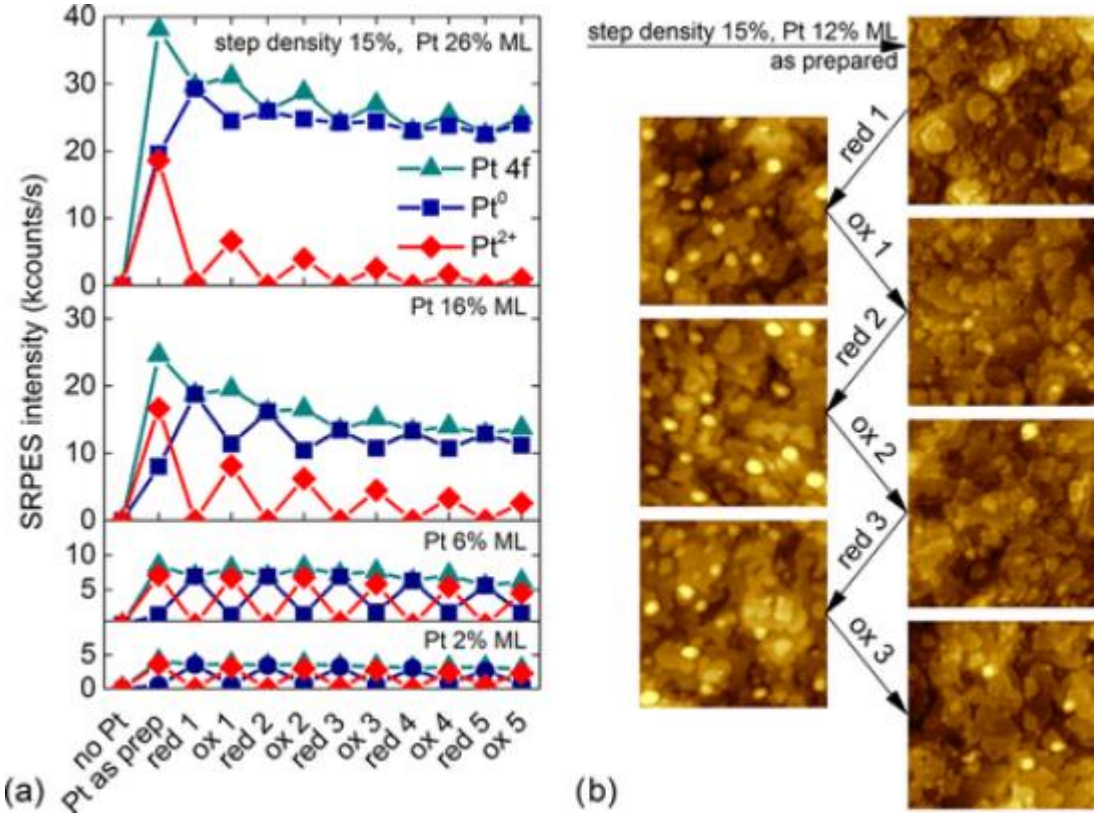

Figure 2. Redispersion and coarsening of Pt load on CeO_2(111) under oxidizing/reducing conditions. Pt was deposited at 300 K and annealed at 700 K in UHV ("Pt as prep") followed by annealing at 600 K in alternating reducing (CH_3OH, "red") and oxidizing (O_2, "ox") conditions. Experiments were performed for Pt

amounts between 2 and 26% ML deposited on CeO_2(111) substrates with 15% ML monoatomic steps. (a) Pt^{2+} (single atoms), Pt^0 (metallic clusters), and total Pt 4f signal in SRPES spectrum. (b) STM images for 12% ML Pt. Occupied state images, 45 × 45 nm^2, sample bias 7.5 V, tunneling current 45 pA.

Parallel to the Pt 4f signal, other SRPES signals were monitored to characterize the chemical state of the samples during reduction and oxidation treatments. The results are shown in Figures S1 and S2. Particularly, the reduction of the CeO_2(111) surface was determined by resonant photoelectron spectroscopy (RPES) via the so-called resonant enhancement ratio (RER) of the Ce valence band (VB) signal. (37) A complete coarsening (suppression of the Pt^{2+} signal) in the reduction cycles was accomplished by reducing the samples to the values of RER >1.0. (32) Upon oxidizing cycles, RER decreases to <0.1 corresponding to almost fully stoichiometric CeO_2(111). (32) Reduced CeO_{2-x}(111) surface is highly reactive toward water and alcohols resulting in strong OH adsorption at the surface (Figure S1g,h). The use of organic reductant (CH_3OH) in the reduction cycles results in the presence of carbonaceous adsorbates at the surface after both reducing and oxidizing cycles (Figure S1d,h,l). This indicates that the redispersion of Pt on ceria-based single-atom catalyst supports is robust with respect to organic and carbonaceous contaminants.

An STM experiment illustrating the morphology of the model Pt/CeO_2(111) samples was performed for 12% ML Pt (0.9 Pt atoms/nm^2, cf. ref (27)) deposited on the CeO_2(111) surface with 15% ML steps. The results are summarized in Figure 2b. On the as-prepared samples with fully redispersed Pt, only (111) terraces and monolayer-high steps of CeO_2(111) surface are apparent. Upon reduction treatment, nanoparticles decorating ceria step edges appear. The observed nanoparticle density corresponds to an average nanoparticle size of 120 Pt atoms. Upon oxidation treatment, the nanoparticles disappear; however, the efficacy of this process seems to be decreasing for the consecutive reduction/oxidation cycles. Pt nanoparticles on the partially reduced CeO_2(111) surfaces were best viewed by STM in occupied states with tunneling voltage increased to 7–8 V. In empty states, STM contrast of the Pt nanoparticles was lower and comparable to the contrast of the OH-terminated, oxygen-deficient CeO_2(111) (Figure S3). STM experiments also confirm that upon both oxidation and reduction treatments the morphology and step density of CeO_2(111) substrates remain unchanged.

The experiments summarized in Figures 1 and 2 reveal a variety of dynamic processes related to redispersion and coarsening of the Pt load on CeO_2(111). A common property of all observed processes is their thermally activated nature. Performing the experiments on flat model CeO_2(111) substrates using surface science methods allowed quantification of the density of available single-atom sites. Many observed processes are influenced by the capacity of the CeO_2(111) surface to accommodate Pt in single-atom traps, i.e., by the ratio of the density of the monoatomic steps on CeO_2(111) to the amount of deposited Pt. Some general phenomena can be identified, e.g., coarsening of Pt nanoparticle populations for the cases when metallic Pt nanoparticles prevail.

Activation Barriers for Filling Pt Single-Atom Traps on CeO_2(111)

Understanding the thermally activated nature of the Pt redispersion on CeO_2 in oxidizing conditions requires considering Pt transport processes on the CeO_2(111) surface at the atomic scale. Pt nanoparticle diffusion can be excluded because single-atom traps at CeO_2(111) step edges must be populated by diffusing species containing single Pt atoms. In some studies, Pt mass transport through gas phase via volatile PtO_2 is invoked. (27,38,39) On geometrically flat model CeO_2(111) substrates, however, a formation and desorption of PtO_2 would lead to a fast removal of Pt deposit, which is not observed. Ab initio calculations predict that due to the small binding energy of the PtO_2 molecule on CeO_2(111), surface diffusion of PtO_2 does not take place. (27) The presence of carbonaceous species on our samples (Figure S1d,h,l) may invoke consideration of Pt transport via Pt carbonyls. (40) This mechanism however cannot account for all observed phenomena, e.g., for the Pt redispersion after deposition (Figures 1 and S1d). Moreover, monodispersed Pt^{2+} ions at ceria step edges do not interact with CO. (31) It seems reasonable to assume a mass transport of Pt on CeO_2(111) surfaces via diffusion of Pt single atoms—adatoms. Theoretical studies predict the binding energy of Pt adatom on CeO_2(111) surface 3.3 eV, (31) and the activation energy for Pt adatom hopping on clean CeO_2(111) surface 0.5 eV, rendering surface diffusion of Pt adatoms a fast and efficient process. (41)

Single-atom traps for Pt adatoms are localized at the step edges of CeO_2(111) (19,27,31,32) and must be occupied by surface diffusion of Pt adatoms from upper or lower CeO_2(111) terraces adjacent to the step edges. This process may account for the experimentally observed thermal activation of Pt redispersion provided that energy barriers preventing adatom attachment at the step edge from the upper or the lower terrace are present. (42,43) Here, we estimate such step-edge barriers for Pt adatom capture at CeO_2(111) monoatomic step edges based on density functional theory (DFT) calculations. (44)

Following our previous works on Pt incorporation and reactivity at CeO_2(111) step edges, (31,32,45) we select two different low-energy step geometries, which we label as Type I and Type II. (46) For each step geometry, we consider both stoichiometric step edges as well as step edges in the presence of excess oxygen atoms decorating the steps (Figure S4). We have previously demonstrated that excess O atoms bind preferentially at step edges leading to the formation of stable peroxide species. (31,32) Peroxide species, in turn, determine the preferential binding of Pt adatoms to the oxidized step edges and increase the Pt binding energy by 1.6 eV with respect to stoichiometric step edges. This large increase in Pt binding energy correlates with the formation of characteristic square-planar PtO_4 units. (31) The adsorption energy of Pt on all of the considered model steps is summarized in Table S1.

To quantify the step-edge barrier for the Pt incorporation at CeO_2(111) step edges via surface diffusion, we have calculated the minimum energy path corresponding to the diffusion of a Pt adatom from a CeO_2(111) terrace to a step edge. This process has been calculated considering diffusion paths from both sides of the step edge (i.e., from the upper and lower terraces), for both model step edges (Type I and Type II), and for different degrees of step-edge oxidation (stoichiometric and with excess oxygen). The minimum energy paths have been computed using the climbing image

nudged elastic band (CI-NEB) method, which provided the activation energy for Pt diffusion at the ceria step edge. A schematic illustration of the calculation for Step Type II with excess oxygen is in Figure 3, and all calculated configurations are summarized in Figure S5.

Figure 3

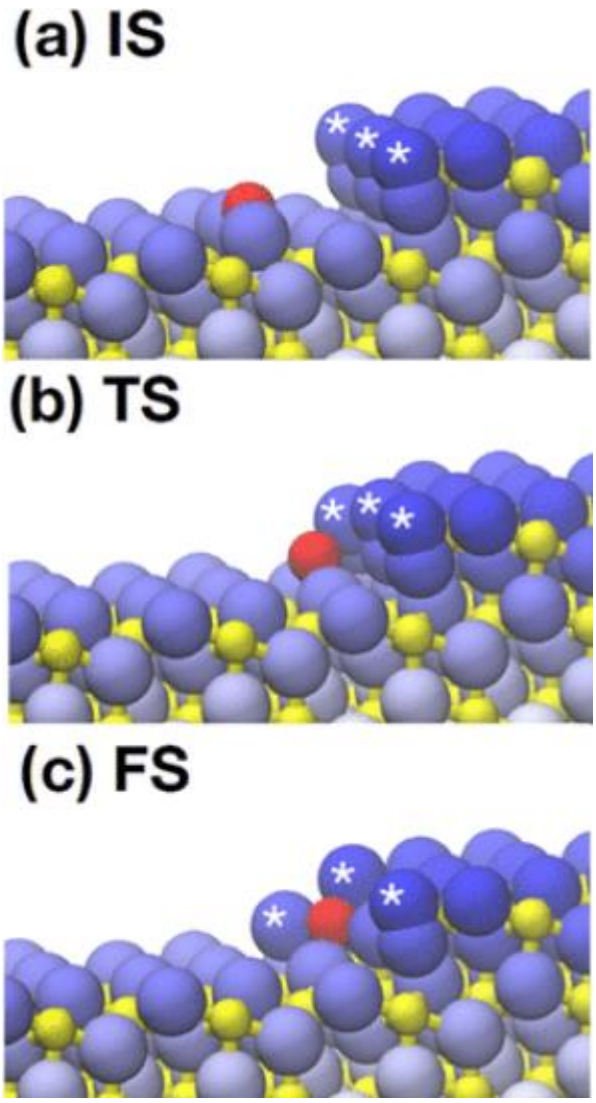

Figure 3. Representative configurations of the calculated minimum energy path for the Pt adatom diffusion and incorporation at Type II Excess Oxygen step edge. (a–c) Initial (IS), transition (TS), and final (FS) states of the process. Pt atom, red; Ce atoms, yellow; O atoms, blue. Excess O atoms are indicated with *.

The resulting step-edge barriers are reported in Table 1. We compare the step edge barriers to the activation energy E_d for Pt diffusion on the stoichiometric CeO_2(111) terrace, E_d = 0.50 eV. For most cases, the activation energies for Pt adatom capture at CeO_2(111) single-atom traps differ from the activation energy of Pt adatom diffusion on the (111) terrace by 0.1 eV or less, where 0.1 eV is the estimated error of the calculation. In one case (Step Type II excess oxygen/lower terrace), Pt diffusion toward the step edge is enhanced, and in another case (Step Type I

stoichiometric/upper terrace), the diffusion requires an additional activation. Still, Steps Type I stoichiometric can be easily occupied from the lower terrace. Overall, we can conclude that the DFT calculations do not predict significant activation barriers for Pt adatom capture in single-atom traps on CeO_2(111).

Table 1. DFT Calculations of Activation Energies for Pt Adatom Capture in Single-Atom Traps on CeO_2(111)

	from lower terrace (eV)	from upper
Step Type I stoichiometric	0.47	0.75
Step Type II stoichiometric	0.59	0.42
Step Type I excess oxygen	0.60	0.60
Step Type II excess oxygen	0.16	0.40

Generic Model of Metal Redispersion and Coarsening on Single-Atom Catalyst Substrates

The absence of the step-edge barrier for Pt adatom capture in single-atom traps on CeO_2(111) step edges resulting from our DFT calculations (Figure 3, Table 1) indicates that Pt adatom capture is a diffusion-limited process and the thermal activation in the present (Figures 1 and 2) and previous experimental observations (19,24,31−33) is rather required to increase the Pt adatom concentration on the samples, and thus Pt adatom availability for a capture. The only source of Pt adatoms on our samples can be Pt nanoparticles. In such a case, Pt distribution on the sample surface must be a result of competition between adatom capture in single-atom traps and adatom capture by Pt nanoparticles.

For the formulation of a model of Pt redispersion and coarsening on CeO_2(111) a suitable description of Pt cohesion in Pt nanoparticles is required. While ab initio calculations of the stability of supported metal clusters and ab initio calculations of the atom detachment from the clusters are available, (47−49) they are restricted to specific cluster geometries and cannot effectively describe the broad range of cluster configurations at elevated temperatures.

We aim at formulating a generic model, i.e., a model replicating the observed Pt redispersion and coarsening phenomena based on a minimum amount of assumptions. In such a case, it is favorable to describe Pt cohesion within the frame of a bond-counting or bond-additivity model, when the energy cost of Pt adatom detachment from a Pt nanoparticle is considered proportional to the number of broken nearest-neighbor Pt−Pt bonds. (50−52) Kinetic Monte Carlo implementations of bond-counting models correctly replicate nucleation and Ostwald ripening of metal nanoparticles (53,54) and can be modified to account for additional kinetic phenomena, e.g., in anisotropic or multicomponent systems. (55,56)

To describe Pt redispersion and coarsening on ceria, we perform kinetic Monte Carlo (KMC) simulations within a bond-counting model on a plain cubic lattice. On the plain cubic lattice, Pt cohesive energy is equal to 3 times the energy of the broken Pt−Pt bond, $E_c = 3 \times E_n$. (57) Ceria substrate is considered immobile and containing single-atom steps. Steps type I and II on CeO_2(111) are represented by {110} steps on the plain cubic lattice. {110} steps correctly replicate the capacity of steps Type I and II to accommodate up to 1 Pt single atom per 1 step site without creating Pt−Pt

bonds, see Figures S6 and S7. The binding energy of the Pt atom at step-edge site can be switched between that corresponding to oxidized step edge E_1^{ox} (Figure S6a) and reduced step edge E_1^{re} (Figure S6b). All Pt adatom hops in the model are assigned the same activation energy E_d, and no additional energy barrier is associated with Pt attachment or detachment to and from the step edges and Pt nanoparticles. Energy parameters of the model are selected in the way that they obey the relationship $E_1^{ox} > E_c > E_1^{re}$ identified in previous ab initio calculations. (31,32) Parameters of the KMC simulation are summarized in Table 2, while the relation of binding energies in the KMC simulation to the results of ab initio calculations is illustrated and discussed in Figure S8.

Table 2. Activation and Binding Energies of Pt Adatom in the KMC Simulations[a]

activation energy	
Pt adatom diffusion	E_d
binding energy	
Pt–Pt nearest-neighbor	E_n
Pt cohesive	E_c
Pt at oxidized step	E_1^{ox}
Pt at reduced step	E_1^{re}

[a] Binding energies are relative to the binding energy of Pt adatom on the oxide surface.

KMC simulations performed within the proposed generic model qualitatively replicate and allow to interpret the experimental data. For the experiment on thermal activation of Pt redispersion presented in Figure 1, we perform KMC simulation depositing 5% ML Pt at 300 K on substrates containing 6, 10, or 17% monoatomic steps. Ceria substrates before Pt deposition are considered partly oxidized, with oxidized and reduced steps each representing 50% of the step-edge sites (Figure S6c). Upon Pt deposition, we simulate 30 s annealing cycles at temperatures 350, 400, ..., 700 K and evaluate the Pt dispersion on the samples at the end of each annealing cycle. In analogy to previous experimental and theoretical studies, (31−33) the intensity of the simulated Pt^{2+} SRPES signal is considered proportional to the amount of isolated Pt adatoms at oxidized steps. All other Pt atoms in the simulation contribute to the intensity of the simulated Pt^0 SRPES signal (Figure S7). For the evaluation of the simulated Pt^0 SRPES signal, the exponential attenuation of the signal from subsurface Pt atoms is taken into account (Figure S7).

The results of the simulation are summarized in Figure 4. At 300 K, E_d of Pt on ceria (0.5 eV) is sufficient for all deposited atoms to reach step edges. With increasing step density and decreasing distance between the steps the probability for the adatom to reach the oxidized step is increasing, resulting in the growing fraction of Pt atoms dispersed as Pt^{2+} ions. Other deposited adatoms reach reduced steps or nucleate small metallic Pt aggregates at step edges (Figure 4b, panels ① and ③). The resulting morphology at 300 K is kinetically limited and a subsequent annealing at progressively higher temperatures brings the system to more energetically favorable configurations, increasing the occupancy of oxidized steps. Upon annealing at 700 K, the dispersion of Pt as Pt^{2+} ions is complete for the samples with

the density of oxidized steps exceeding the amount of deposited Pt (Figure 4b, panel ②), and maximized for the sample with the density of oxidized steps lower than the amount of deposited Pt (Figure 4b, panel ④). At temperatures between 400 and 550 K, an accelerated transient to the Pt^{2+} state is observed that can be attributed to thermal activation of characteristic system configurations, particularly Pt atoms with two nearest neighbors, and Pt atoms in shallow single-atom traps (cf. Figure 4b, panel ③).

Figure 4

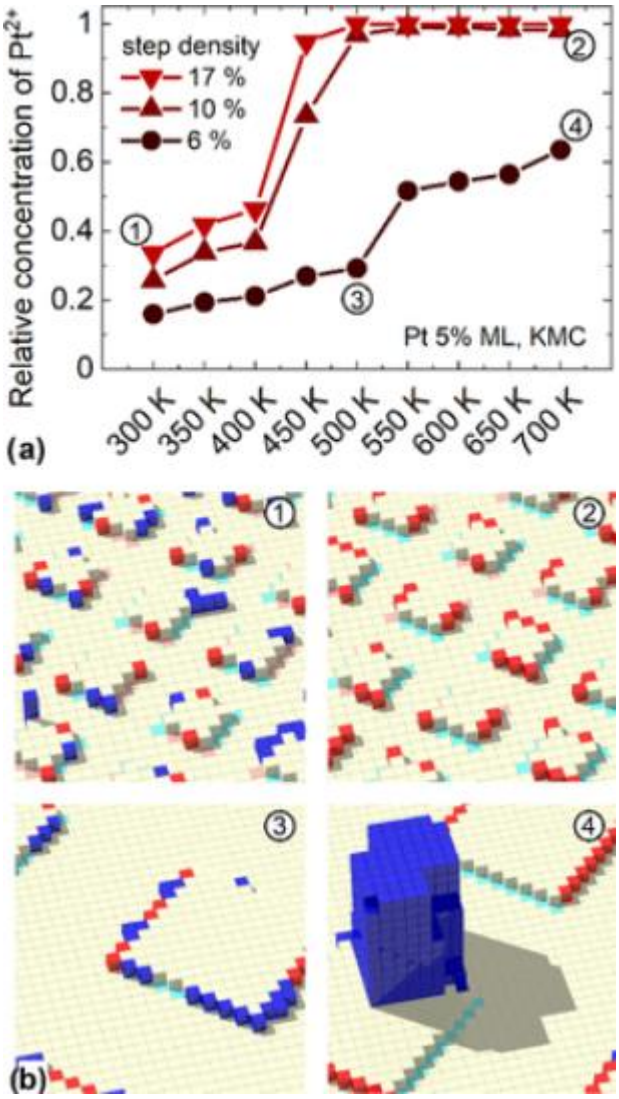

Figure 4. KMC simulation of Pt redispersion in single-atom traps. (a) Pt deposition at 300 K and intermittent annealing to gradually increasing temperatures. (b) KMC morphologies corresponding to the points ①–④ in (a). Color coding: red, Pt^{2+} ions; blue, metallic Pt; pink, oxidized step; cyan, reduced step.

The KMC simulations clearly illustrate that the thermal activation required for redispersion of the Pt load on CeO_2(111) is due to kinetic limitations preventing Pt adatoms from reaching oxidized step edges rather than due to the microscopic nature of the interactions between Pt adatoms and steps (cf. Table 1). Assuming a

sufficient thermal activation, we now attempt at simulating Pt coarsening and redispersion in reducing and oxidizing conditions (Figure 2). On CeO_2(111), changes in the oxygen content at monolayer step edges result in the changes of binding energy of Pt single atoms—from low E_1^{re} at oxygen deficiency to high E_1^{ox} at oxygen surplus and vice versa (Tables S1 and 2). (31,32)

The results of the KMC simulation are summarized in Figure 5. Simulations were performed on substrates containing 10% of monolayer-high steps and Pt deposit amounts 10% ML (Figure 5a,b) and 20% ML (Figure 5c,d). Pt was deposited at 300 K and redispersed at temperature 550 K for 200 s under oxidizing conditions (all steps oxidized, Figure S6b). Afterward, the temperature was kept at 550 K and the substrate condition was alternated in 200 s time intervals between reduced (Figure S6a) and oxidized (Figure S6b). At the end of each time interval, simulated Pt signals (Pt^{2+}, Pt^0) and system morphology were evaluated.

Figure 5

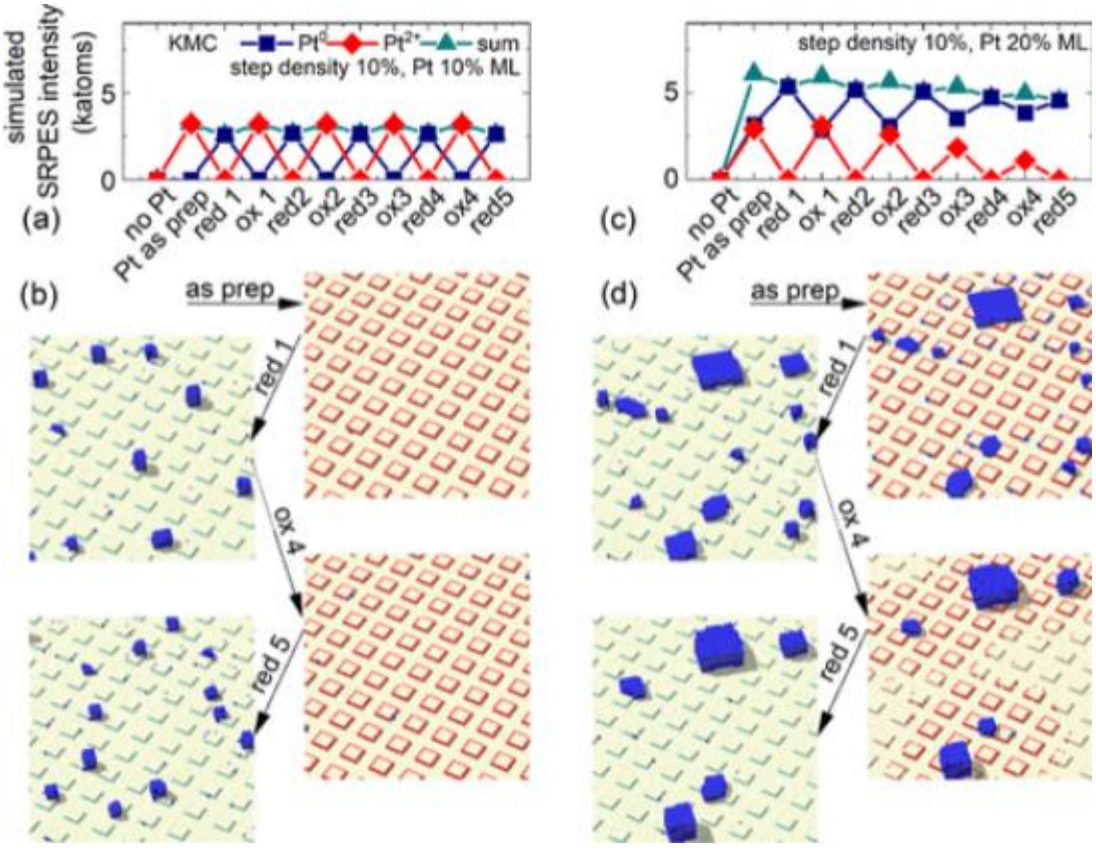

Figure 5. KMC simulation of redispersion and coarsening of Pt load. Redispersion and coarsening are induced by alternatingly switching the step edges from oxidized to reduced. Step density 10% ML, Pt amount (a, b) 10% ML, (c, d) 20% ML. (a, c) Single-atom (Pt^{2+}), metallic (Pt^0), and Pt total ("sum") simulated SRPES signal. (b, d) KMC morphologies. Color coding: red, Pt^{2+} ions; blue, metallic Pt; pink, oxidized step; cyan, reduced step.

In both calculations, we observe a qualitative replication of the dynamic phenomena identified in the experiment (Figure 2a): coarsening and redispersion of the Pt

deposit upon reduction (“red1”–“red5”) and oxidation treatments (“ox1”–“ox4”), and corresponding changes of the Pt^0, Pt^{2+}, and total Pt 4f signals. For a Pt amount comparable to the step density (10% ML Pt), Pt redispersion on the as-prepared samples (“Pt as prep”) is almost complete, and subsequent coarsening is very reversible. For Pt amount larger than the step density (20% ML Pt), Pt redispersion on the as-prepared samples is incomplete and subsequent coarsening and redispersion cycles exhibit progressive growth of metallic Pt nanoparticles at the expense of atomically dispersed Pt. Simulated morphologies correspond to the morphology observed in STM (Figure 2b) and provide a real space illustration of the observed dynamic phenomena.

Stable and Unstable Nanoparticle Distributions within the Generic Model

Obtaining a qualitative agreement between experimental and simulated data on adatom and nanoparticle dynamics allows us to investigate conditions for stable and unstable nanoparticle populations within the proposed generic model. Under stationary oxidizing conditions, the parameter determining stability or instability of the resulting Pt population is the density of the oxidized steps ρ^{ox}. A trivial stable solution is obtained for Pt amount $\rho^{Pt} \leq \rho^{ox}$ when, ultimately, all Pt is redispersed as single atoms. A nontrivial stable solution is obtained for Pt amount slightly exceeding ρ^{ox}, $\rho^{Pt} = \rho^{ox} + \varepsilon$. This solution is illustrated in Figure 6a. We simulate redispersion of Pt clusters of average size ~80 atoms under oxidizing conditions and at 550 K. Redispersion is complete after 400 s. Afterward, Pt population remains stable until 3600 s. Pt atoms exceeding the capacity of oxidized steps remain highly dispersed, forming subcritical 2D Pt^0 clusters with a prevailing size of 3 Pt atoms (see Figure 6b).

Figure 6

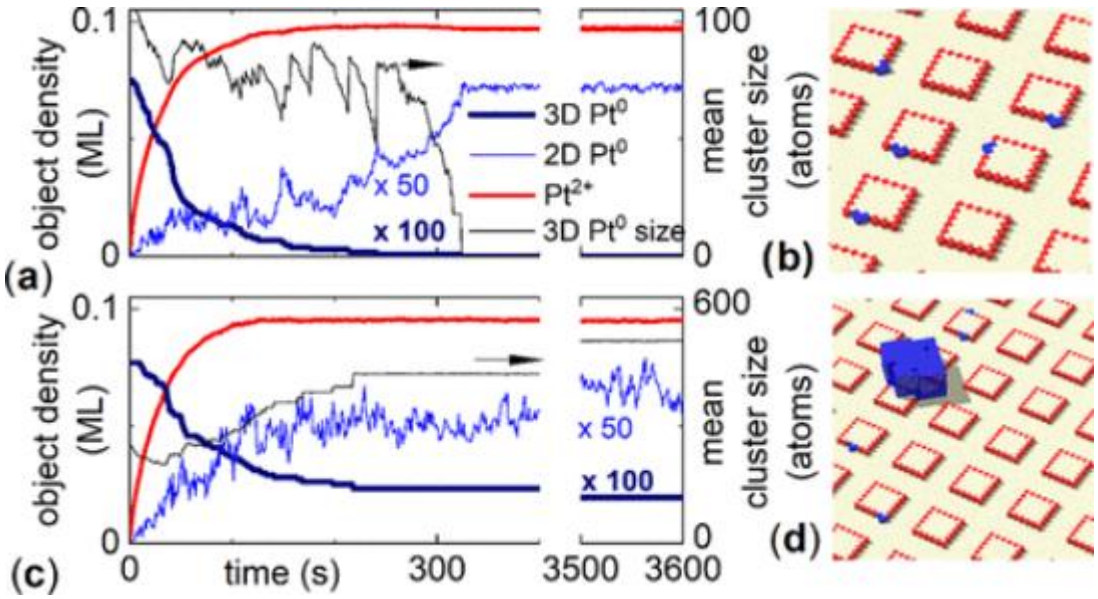

Figure 6. KMC simulations of stable (a, b) and unstable (c, d) nanoparticle populations upon redispersion of 3D Pt clusters at stationary oxidizing conditions. Step density 10% ML, Pt amount (a, b) (10 + ε)% ML, ε = 0.15% ML, (c, d) 15% ML. (a,

c) Time evolution of density of Pt^{2+} single atoms, subcritical 2D Pt^0 clusters, 3D Pt^0 clusters, and average 3D Pt^0 cluster size. (b, d) KMC morphologies at 3600 s.

In the present discussion, and in Figures 6 and 7, we evaluate the density of the subcritical 2D Pt^0 clusters separately from the density and average size of the 3D Pt^0 clusters. Subcritical clusters originate from an attachment of Pt adatoms to oxidized steps decorated by Pt^{2+}, and, given the density of subcritical clusters, the size distribution of metallic Pt nanoparticles in the model (3D clusters + 2D subcritical clusters) must be considered bimodal. The existence, morphology, and metallic character of the subcritical clusters are rationalized by previous DFT studies of Pt structures on ceria step edges. (31,32) The density of subcritical clusters on the surface reflects in part the intensity of Pt surface mass transport, cf. the correlated character of the fluctuations of the average nanoparticle size and the density of subcritical clusters in Figure 6a. Subcritical clusters can be generally considered to provide different chemical reactivity compared to Pt single atoms in deep traps or to 3D Pt nanoparticles. (26)

Figure 7

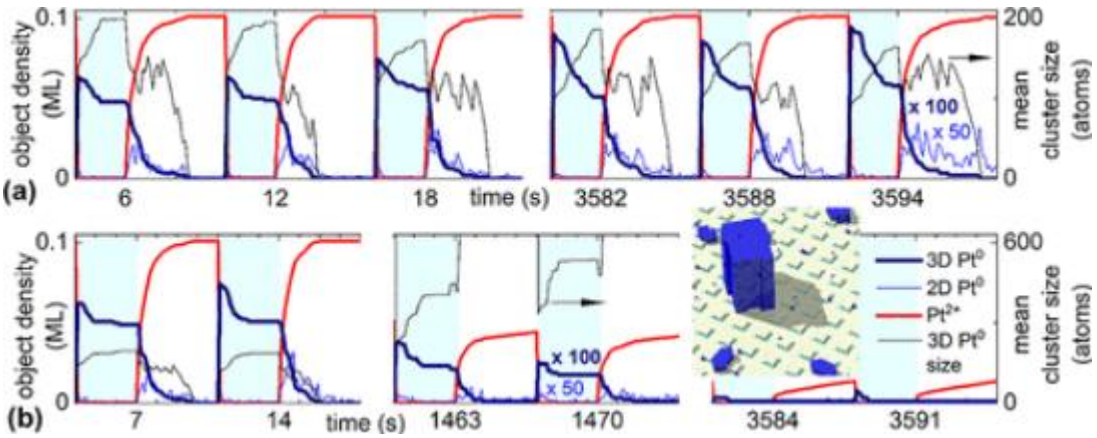

Figure 7. KMC simulations of stable (a) and unstable (b) nanoparticle populations during alternating oxidizing/reducing conditions. Step density 17% ML, Pt amount 10% ML. Cycle times: (a) 2 s reduction, 4 s oxidation (b) 3 s reduction, 4 s oxidation. Reduction cycles are highlighted in light blue. Inset in (b): KMC morphology at 1470 s.

Unstable nanoparticle distributions at stationary oxidizing conditions are obtained for $\rho^{Pt} > \rho^{ox} + \varepsilon$. The situation is illustrated in Figure 6c,d. We simulate redispersion of Pt nanoparticles of average size ~500 atoms under oxidizing conditions and at 550 K. After 400 s, the Pt^{2+} population at oxidized steps is maximized. The redispersion is however incomplete since Pt exceeding the capacity of single-atom traps remains on the surface in the form of 3D clusters (Figure 6d). The 3D clusters undergo Ostwald ripening and cause the unstable character of the Pt population with nanoparticle density and mean nanoparticle size changing at times of 3600 s (Figure 6c) and beyond.

At stationary reducing conditions, only an unstable solution is available. The 3D clusters undergo Ostwald ripening which is, in the absence of additional constraints on characteristic system sizes, (58,59) a nonstationary process. (60)

In alternating oxidizing/reducing conditions, the stability of the nanoparticle populations requires, in addition to sufficient ρ^{ox}, a suitable timing. We perform KMC simulations of the nanoparticle population for ρ^{Pt} = 10% ML, and ρ^{ox} = 17% ML ($\rho^{Pt} < \rho^{ox}$), and at simulation temperature 650 K, when the redispersion and coarsening times are reduced to an order of single seconds, comparable to, e.g., alternating oxidizing/reducing conditions in three-way automotive catalytic converters. (61,62) Oxidizing and reducing conditions are simulated as in the calculations presented in Figure 5—all step-edge traps are set oxidized (Figure S6b) or reduced (Figure S6a).

A stable nanoparticle population can be obtained for alternating 2 s reduction cycles and 4 s oxidation cycles as illustrated in Figure 7a for simulation times up to 3600 s. Within each oxidation cycle, a complete redispersion of Pt deposit at oxidized steps is obtained. Within reduction cycles, Pt nanoparticles are formed via nucleation and coarsening of Pt adatoms released upon the change from oxidized steps to reduced steps.

Increasing the duration of the reduction cycles to 3 s while keeping the oxidation cycles at 4 s leads to an unstable nanoparticle population, as illustrated in Figure 7b. The breakdown of the stable nanoparticle population is triggered by an incomplete redispersion of Pt in one particular oxidation cycle. This has a consequence of Pt nanoparticles remaining on the surface at the beginning of the next reduction cycle (cf. Figure 5d). Pt adatoms released upon the change from oxidized steps to reduced steps are then preferentially captured at the remaining Pt nanoparticles, resulting in their fast coarsening (see the inset of Figure 7b) and the breakdown of the nanoparticle population, within the spatial limits of KMC simulations, toward the fastest growing single Pt particle. Once this process has started, it cannot be reverted by the intermittent 4 s oxidation cycles. For restoring the complete redispersion, oxidation/reduction cycling must be interrupted and a sufficiently long treatment in oxidizing conditions applied.

Implications of the Generic Model for Real Pt/Ceria Catalysts

The presented view of Pt redispersion and coarsening on ceria as a competition for Pt adatoms between single-atom traps at ceria step edges and Pt nanoparticles can be, in many cases, applied to real ceria catalysts. Monoatomic step edges are ubiquitous on well-annealed nanoparticulate and nanoporous ceria supports, (19,27,63,64) strong bonding of Pt^{2+} has been reported also on (001) nanofacets of ceria nanoparticles. (33) Excess O atoms at ceria step edges required for strong bonding of single Pt^{2+} ions are present already under the conditions of model UHV experiments. (31,32) Excess O in the form of peroxo and superoxo species is readily observed and available for Pt^{2+} stabilization also on real ceria catalysts in air or in lean, oxygen-containing reaction mixtures. (65−67) As is the case of model experiments, monoatomic step edges on real Pt/ceria catalysts exhibit limited capacity to accommodate single Pt^{2+} species during high-temperature treatment in air. Full Pt dispersion to Pt^{2+} species was observed for $\rho^{ox} > \rho^{Pt}$. For $\rho^{ox} < \rho^{Pt}$, saturation of step edges was observed, resulting in the coexistence of isolated Pt^{2+} species and

Pt nanoparticles. (27) Data from ref (27) indicate that ρ_{ox} in the real Pt/ceria catalyst is approximately 1 nm^{-2} or 13% ML, closely matching the presented model experiments (Figures 1, 2, 4, and 5). In real Pt/ceria catalysts, mass transport of Pt on ceria surface via Pt adatom diffusion can be efficient at lower temperatures and within the surface of individual ceria nanoparticles as observed e.g., by TEM. (22) At higher temperatures, or for Pt transport among the ceria nanoparticles, a sublimation of PtO_2 species and Pt mass transport through gas phase may be invoked. (27,38) The efficacy of mass transport via volatile PtO_2 in real catalysts may however need verification by further experiments, e.g., to determine its substrate dependence when Pt load seems unstable on alumina (68) and stable on ceria. (59,61)

The change from oxidizing conditions to reducing conditions in the presented model is considered instantaneous (Figure S6). In real catalysts, a chemical reaction in oxygen-deficient rich reducing reaction mixture must proceed via the removal of O atoms (excess O or lattice O) from Pt^{2+} complexes at step edges. This reaction is expected to proceed fastest at the Pt^{2+} complexes, and at superoxo, peroxo, and lattice O sites at ceria step edges, since the binding energies of O at these sites are smaller than on the facets of ceria nanoparticles. (31,69) The amount of removed oxygen atoms required to deactivate all Pt^{2+} traps at ceria step edges and to initiate nucleation and growth of Pt nanoparticles is on the order of monoatomic step density, i.e., 10% of surface Ce atoms. (32) With bulk sensitive experimental methods employed for characterization of Pt/ceria catalysts under reaction conditions, such amounts of removed O or reduced Ce^{3+} may be difficult to detect and the deactivation of Pt^{2+} traps under reducing conditions can happen before the reduction of ceria bulk is observed. (23)

Apart from single Pt atoms in Pt^{2+} chemical state and metallic Pt nanoparticles, some studies on real Pt/ceria catalysts report one-dimensional (1D) and two-dimensional (2D) Pt objects of oxidized or mixed oxidized/metallic chemical state and a specific catalytic activity different from single Pt^{2+} ions or metallic Pt nanoparticles. (26) Our model suggests that such objects may be related to ceria step edges densely populated with Pt^{2+} ions or to 2D Pt objects at step edges (Figure 6b). 2D decoration of ceria step edges with Pt in a mixed oxidized/metallic chemical state has been proposed earlier based on ab initio calculations. (32)

The generic model of Pt redispersion and coarsening introduced in this work defines and considers a minimal set of kinetic processes required for a qualitative replication of nanoparticle dynamics phenomena on single-atom catalyst substrates and for a general classification of stability of nanoparticle population under stationary or alternating oxidation and reduction conditions. For future quantitative predictions of the evolution of supported nanoparticle size in real catalysts and reaction mixtures, further details of the involved kinetic processes must be clarified at atomic scale. A prerequisite would be an implementation of the KMC simulation on an FCC lattice including kinetic processes relevant to FCC Pt nanoparticle equilibration. (54,57) In the present model, the interaction of the catalyst with oxidizing or reducing atmospheres is influencing only the properties of the single-atom traps. In reality, Pt mass transport across the ceria surface, nucleation of Pt nanoparticles, and the rate of Pt nanoparticle growth or disintegration may vary substantially as a function of concentration of O vacancies, reactants, intermediates,

or products on ceria and Pt nanoparticle surfaces. (70−72) This is corroborated by recent experiments on real Pt/ceria catalysts that reveal a strong influence of the composition of rich reaction mixtures on the activation of Pt/ceria catalysts by redispersion. (22,23) Sensitivity of the redispersion and coarsening processes to the composition of reaction mixtures provides a broad range of topics for further dedicated studies of adatom and nanoparticle dynamics on single-atom catalyst substrates. Further dedicated studies will be also required to investigate the dynamics of activation and deactivation of single-atom traps in alternating oxidizing and reducing atmospheres, and the resulting surface inhomogeneity when oxidized and reduced traps coexist.

Conclusions

Based on surface science studies and DFT analysis of Pt adatom and nanoparticle dynamics on CeO_2(111) surface, we have formulated a generic model of metal redispersion and coarsening on single-atom catalyst substrates. The model comprises fast Pt adatom diffusion and adatom interaction with single-atom traps at CeO_2(111) monoatomic step edges, and with Pt nanoparticles on the catalyst substrate. Activation barriers inherent to Pt redispersion and coarsening on ceria-based single-atom catalyst substrates are associated with transitions of the morphology of supported Pt to energetically favorable configurations—Pt clusters for reducing conditions when single-atom traps on ceria are inefficient, and redispersed Pt single atoms for oxidizing conditions when single-atom traps provide strong bonding to Pt atoms. Besides surface science experiments, our generic model provides atomic-level insight into many nanoparticle dynamics phenomena observed in real Pt/ceria catalysts.

We have delimited the conditions, in terms of the Pt loading and the density of single-atom traps, under which oxidation and reduction treatments of metal deposits on single-atom catalyst substrates can be efficiently utilized in tailoring the morphology of both highly dispersed metal single atoms and metal nanoparticles on demand of a particular catalytic application. We have shown that for long-term activity in catalytic applications, single-atom catalyst substrates provide the possibility of efficient redispersion of supported metal nanoparticles upon activation of single-atom traps under oxidizing conditions. This represents a particularly appealing strategy for catalysts operating in alternating oxidation/reduction atmospheres, such as three-way automotive catalysts. To stabilize the nanoparticle population on a long-term basis, redispersion must be complete in each oxidation cycle. This requires providing sufficient density of single-atom traps to accommodate the metal load and proper timing for the redispersion to complete.

Methods

Experimental Procedures

Experiments were performed at the Materials Science Beamline at the Elettra Synchtrotron in Trieste, Italy (XPS, SRPES, RPES), and in the laboratories of Department of Surface and Plasma Science at Charles University in Prague, Czech Republic (XPS, STM). Experiments were performed at UHV apparatuses using

procedures described in detail in our previous publications. (31,32) Particularly, CeO_2(111) thin films were prepared by evaporation of Ce metal (Goodfellow, 99.95%) from Mo or Ta crucible on Cu(111) surfaces (MaTecK) in 5×10^{-5} Pa O_2 (Linde, SIAD, 4.7). The density of monoatomic steps was controlled via deposition temperature, reduction/oxidation procedures, or postdeposition annealing as summarized in Table S2. The density of monoatomic steps was determined from STM images via superimposing a manual outline of step edges onto a properly scaled and oriented mesh of surface Ce atoms on CeO_2(111), and counting the number of Ce atoms at lower step edges. (31,32) Pt (Safina, Goodfellow, 99.95%) was deposited at 300 K, and the amount of deposited Pt was controlled via a combination of quartz crystal microbalance (QCM) and XPS measurements of the attenuation of Ce 3d or Cu $2p_{3/2}$ signals. (31,32)

Upon Pt deposition, redispersion to Pt^{2+} was performed by annealing in UHV at 700 K or lower as described in the text (Figure 1). Reduction treatments of the samples were performed via 1 min annealing of the samples in 1×10^{-5} Pa CH_3OH at 600 K. Reduction treatments were repeated, eventually, until the ceria reduction indicated by RER (Figure S1b,f,j) increased above 1.0. Oxidation treatments of the samples were performed via 10 min exposure to 1×10^{-5} Pa O_2 at 300 K followed by flash annealing at 600 K in the same O_2 background. Oxidation treatments were repeated, eventually, until RER decreased below 0.1. After the oxidation, the samples were flash-annealed at 700 K in UHV.

In between the redispersion/reduction/oxidation steps, the oxidation state of Pt deposit and ceria support was characterized at 300 K by XPS, SRPES, and RPES. An overview of the evaluated data and the corresponding fitting and background subtraction are presented in Figures S1 and S2. STM experiments were performed at 300 K using a mechanically cut Pt–Ir STM tip. Complementary images of occupied states and empty states were obtained (Figures 2b and S3).

DFT Calculations

All calculations were based on the DFT employing ultrasoft pseudopotentials and the Perdew, Burke, and Ernzerhof (PBE) generalized gradient-corrected approximation for the exchange and correlation functional. (73,74) The electronic wave function and density were described with a plane-wave basis set employing energy cutoffs of 40 and 320 Ry, correspondingly. Following the established practice, we use the PBE+*U* approach to describe the electronic structure of ceria-based materials, employing the implementation of Cococcioni and de Gironcoli (75) which includes an additional Hubbard-*U* term to the Kohn–Sham functional that disfavors fractional occupancies of the Ce 4f states. The value of the parameter *U* was set to 4.5 eV. (76) All calculations have been performed using the Quantum-ESPRESSO computer package. (77) The minimum energy paths at 0 K have been computed using the CI-NEB algorithm using a Broyden scheme as implemented in the Quantum-ESPRESSO package. The reaction path was sampled with 8–12 intermediate images.

The adsorption of Pt atoms at ceria step edges was modeled with periodic supercells describing vicinal surfaces. Two of the lowest energy model steps proposed in ref (46) have been selected. Following this work, we label our two model step surfaces as Step Type I and Step Type II. In both models, the step edge exposes

three independent O atoms. The step edge is separated by two (111) terraces and is oriented along the [110] direction. The lateral dimensions for the supercells are 17.97 Å × 11.67 Å and 15.72 Å × 11.67 Å for Steps Type I and II, respectively, along the [112] and [110] directions. The supercell slabs comprised nine atomic layers and their surfaces were separated by more than 11 Å of vacuum in the direction perpendicular to the (111) terrace. During the structural relaxation, the lowest three atomic O–Ce–O layers were constrained to their bulk equilibrium coordinates, as well as the Ce atoms in the central O–Ce–O trilayers far from the step edge.

KMC Simulation

We adapt a solid-on-solid (no vacancies, no overhangs) KMC model on a cubic lattice with a periodic boundary condition. (51) The model is implemented within the Bortz–Kalos–Lebowitz algorithm (78) allowing us to set the simulation temperature and evaluate the simulation time. We consider mobile adatoms of the deposit (Pt) on substrates with fixed stepped geometry (ceria). Lattice parameters of the substrate and deposit are the same, i.e., no strain is considered. Pt–Pt interactions are approximated by a bond-counting scheme. (50) To account for the 3D character of Pt nucleation, both lateral and vertical Pt–Pt bonds are considered. Pt nucleation in the model is spontaneous, without defining a critical nucleus. (79) Geometry and bonding properties of monoatomic steps on the substrates in the simulation (Figure S6) are defined in a way that the interaction of Pt adatoms with adatom traps at lower step edges corresponds to the experimentally and theoretically determined interaction of Pt adatoms with monoatomic steps on CeO_2(111). (31,32) Activation and binding energies in the model are summarized in Table 2. Binding energies in the model are scaled with respect to binding energies predicted by ab initio calculations (Figure S8 and Supporting Discussion). This results in an effective shifting of the temperature scale of the simulation to lower values compared to the experiment. Rescaling the activation energies in KMC allowed to obtain manageable computing times in the range of weeks for a 3600 s simulation (Figures 6 and 7) on a single core.

The activation energy of Pt adatom hopping in the model is defined for four different situations: $E_a^{Pt\rightarrow Pt}$, $E_a^{Pt\rightarrow Ce}$, $E_a^{Ce\rightarrow Ce}$, and $E_a^{Ce\rightarrow Pt}$, depending on the type of the underlying atom to the Pt adatom before and after the hop. The 3D character of Pt growth is obtained by assigning the $E_a^{Pt\rightarrow Ce}$ hops one more broken bond—the vertical one. Activation energies for Pt hopping in the model are determined as follows: $E_a^{Pt\rightarrow Pt} = E_d + n\,E_n$, $E_a^{Pt\rightarrow Ce} = E_d + (n+1)\,E_n$, $E_a^{Ce\rightarrow Ce} = E_a^{Ce\rightarrow Pt} = E_d + n\,E_n + \delta_{i1}E_1^{ox} + \delta_{i2}E_1^{re}$, where E_d is the activation energy for Pt adatom diffusion both on ceria and on Pt, E_n is the energy associated with breaking a Pt–Pt nearest-neighbor bond, n is the number of lateral Pt–Pt nearest neighbors before the hop (n = 0, ..., 4), and i is the type of the step edge underlying the Pt adatom before the hop (i = 0, 1, 2 for none, oxidized and reduced step, respectively). Hopping frequencies are evaluated in a standard way, $\nu_x = \nu_0 \exp(-E_a^x/k_BT)$, where $\nu_0 = 10^{13}$ s^{-1}, k_B is the Boltzmann constant, and E_a^x is the activation energy of an x-th process.

The charge state of Pt in the simulation, and the simulated Pt^{2+} and Pt^0 SRPES signals are determined based on the local geometry of Pt atoms in the simulation according to previous experimental and theoretical findings (31,32) as described in

Figure S7. Experimental cycles of annealing in UHV, reducing, and oxidizing conditions are simulated by instantaneous switching of the binding energy of the step-edge traps in the model from deep to shallow or vice versa (cf. Figure S6). Evaluation of KMC configurations is performed at the end of particular simulation cycles without simulating the cooldown to 300 K and a subsequent heating up for the next cycle. Initial KMC configurations for the presented calculations are obtained in analogy to the experimental treatments by simulated deposition and annealing cycles. Parameters of the presented KMC simulations are summarized in Table S3.

Supporting Information

The Supporting Information is available free of charge at https://pubs.acs.org/doi/10.1021/acscatal.2c00291.

- Acquisition and processing of experimental data, step-edge geometries considered in DFT, and energy scale and geometry of the KMC model (PDF)

Acknowledgments

F.D., V.J., and J.M. acknowledge the support of the Czech Science Foundation, project No. 20-11688J. F.D., M.V., I.K., T.S., and I.M. acknowledge Ministry of Education (LM2018116), the Czech Science Foundation (project No. 20-13573S) for financial support, and the CERIC-ERIC Consortium for the access to experimental facilities. This project has received funding from the EU-H2020 research and innovation program (grant number 654360). NFFA-Europe provided access to the CNR-IOM theory facility within the framework of the NFFA Transnational Access Activity.

References

1. **1**
Van Santen, R. A. Complementary Structure Sensitive and Insensitive Catalytic Relationships. *Acc. Chem. Res.* **2009**, *42*, 57– 66, DOI: 10.1021/ar800022m

2. **2**
Roldan Cuenya, B.; Behafarid, F. Nanocatalysis: Size- and Shape-Dependent Chemisorption and Catalytic Reactivity. *Surf. Sci. Rep.* **2015**, *70*, 135– 187, DOI: 10.1016/j.surfrep.2015.01.001

3. **3**
Yang, J. H.; Henao, J. D.; Raphulu, M. C.; Wang, Y.; Caputo, T.; Groszek, A. J.; Kung, M. C.; Scurrell, M. S.; Miller, J. T.; Kung, H. H. Activation of Au/TiO_2 Catalyst for CO Oxidation. *J. Phys. Chem. B* **2005**, *109*, 10319– 10326, DOI: 10.1021/jp050818c

4. **4**
Juan-Juan, J.; Román-Martínez, M. C.; Illán-Gómez, M. J. Nickel Catalyst Activation in the Carbon Dioxide Reforming of Methane. *Appl. Catal., A* **2009**, *355*, 27– 32, DOI: 10.1016/j.apcata.2008.10.058

5. **5**
Newton, M. A. Dynamic Adsorbate/Reaction Induced Structural Change of Supported Metal Nanoparticles: Heterogeneous Catalysis and Beyond. *Chem. Soc. Rev.* **2008**, *37*, 2644, DOI: 10.1039/b707746g

6. **6**
Liu, L.; Corma, A. Evolution of Isolated Atoms and Clusters in Catalysis. *Trends Chem.* **2020**, *2*, 383– 400, DOI: 10.1016/j.trechm.2020.02.003

7. **7**
Morgan, K.; Goguet, A.; Hardacre, C. Metal Redispersion Strategies for Recycling of Supported Metal Catalysts: A Perspective. *ACS Catal.* **2015**, *5*, 3430– 3445, DOI: 10.1021/acscatal.5b00535

8. **8**
Nagai, Y.; Dohmae, K.; Ikeda, Y.; Takagi, N.; Tanabe, T.; Hara, N.; Guilera, G.; Pascarelli, S.; Newton, M. A.; Kuno, O.; Jiang, H.; Shinjoh, H.; Matsumoto, S. In Situ Redispersion of Platinum Autoexhaust Catalysts: An On-Line Approach to Increasing Catalyst Lifetimes?. *Angew. Chem., Int. Ed.* **2008**, *47*, 9303– 9306, DOI: 10.1002/anie.200803126

9. **9**
Liu,J.CatalysisbySupportedSingleMetalAtoms.*ACSCatal.***2017**,*7*,34–59,DOI:10.1021/acscatal.6b01534

10. **10**
Liu,L.;Corma,A.MetalCatalystsforHeterogeneousCatalysis:FromSingleAtomstoNanoclustersandNanoparticles.*Chem.Rev.***2018**,*118*,4981–5079,DOI:10.1021/acs.chemrev.7b00776

11. **11**
Yang,X.;Wang,A.;Qiao,B.;Li,J.;Liu,J.;Zhang,T.Single-AtomCatalysts:ANewFrontierinHeterogeneousCatalysis.*Acc.Chem.Res.***2013**,*46*,1740–1748,DOI:10.1021/ar300361m

12. **12**
Flytzani-Stephanopoulos,M.GoldAtomsStabilizedonVariousSupportsCatalyzetheWater-GasShiftReaction.*Acc.Chem.Res.***2014**,*47*,783–792,DOI:10.1021/ar4001845

13. **13**
Rossell,M.D.;Caparrós,F.J.;Angurell,I.;Muller,G.;Llorca,J.;Seco,M.;Rossell,O.Magnetite-SupportedPalladiumSingle-AtomsDoNotCatalysetheHydrogenationofAlkenesbutSmallClustersDo.*Catal.Sci.Technol.***2016**,*6*,4081–4085,DOI:10.1039/C6CY00596A

14. **14**
Zhou,X.;Yang,W.;Chen,Q.;Geng,Z.;Shao,X.;Li,J.;Wang,Y.;Dai,D.;Chen,W.;Xu,G.;Yang,X.;Wu,K.StablePtSingleAtomsandNanoclustersonUltrathinCuOFilmandTheirPerformancesinCOOxidation.*J.Phys.Chem.C***2016**,*120*,1709–1715,DOI:10.1021/acs.jpcc.5b11362

15. **15**
Goodman,E.D.;Johnston-Peck,A.C.;Dietze,E.M.;Wrasman,C.J.;Hoffman,A.S.;Abild-Pedersen,F.;Bare,S.R.;Plessow,P.N.;Cargnello,M.CatalystDeactivationviaDecompositionintoSingleAtomsandtheRoleofMetalLoading.*Nat.Catal.***2019**,*2*,748–755,DOI:10.1038/s41929-019-0328-1

16. **16**
Maurer,F.;Jelic,J.;Wang,J.;Gänzler,A.;Dolcet,P.;Wöll,C.;Wang,Y.;Studt,F.;Casapu,M.;Grunwaldt,J.-D.TrackingtheFormation,FateandConsequenceforCatalyticActivityofPtSingleSitesonCeO$_2$.*Nat.Catal.***2020**,*3*,824–833,DOI:10.1038/s41929-020-00508-7

17. **17**
Bliem,R.;vanderHoeven,J.E.S.;Hulva,J.;Pavelec,J.;Gamba,O.;deJongh,P.E.;Schmid,M.;Blaha,P.;Diebold,U.;Parkinson,G.S.DualRoleofCOintheStabilityofSubnanoPtClustersattheFe$_3$O$_4$(001)Surface.*Proc.Natl.Acad.Sci.U.S.A.***2016**,*113*,8921–8926,DOI:10.1073/pnas.1605649113

18. **18**
Farmer,J.A.;Campbell,C.T.CeriaMaintainsSmallerMetalCatalystParticlesbyStrongMetal-SupportBonding.*Science***2010**,*329*,933–936,DOI:10.1126/science.1191778

19. **19**
Jones,J.;Xiong,H.;DeLaRiva,A.T.;Peterson,E.J.;Pham,H.;Chala,S.R.;Qi,G.;Oh,S.;Wiebenga,M.H.;Hernández,X.I.P.;Wang,Y.;Datye,A.K.ThermallyStableSingle-AtomPlatinum-on-CeriaCatalystsviaAtomTrapping.*Science***2016**,*353*,150–154,DOI:10.1126/science.aaf8800

20. **20**
Resasco,J.;DeRita,L.;Dai,S.;Chada,J.P.;Xu,M.;Yan,X.;Finzel,J.;Hanukovich,S.;Hoffman,A.S.;Graham,G.W.;Bare,S.R.;Pan,X.;Christopher,P.UniformityIsKeyinDefiningStructure–FunctionRelationshipsforAtomicallyDispersedMetalCatalysts:TheCaseofPt/CeO$_2$.*J.Am.Chem.Soc.***2020**,*142*,169–184,DOI:10.1021/jacs.9b09156

21. **21**
Lu,Y.;Zhou,S.;Kuo,C.-T.;Kunwar,D.;Thompson,C.;Hoffman,A.S.;Boubnov,A.;Lin,S.;Datye,A.K.;Guo,H.;Karim,A.M.UnravelingtheIntermediateReactionComplexesandCriticalRoleofSupport-DerivedOxygenAtomsinCOOxidationonSingle-AtomPt/CeO$_2$.*ACSCatal.***2021**,*11*,8701–8715,DOI:10.1021/acscatal.1c01900

22. **22**
Gänzler,A.M.;Casapu,M.;Vernoux,P.;Loridant,S.;CadeteSantosAires,F.J.;Epicier,T.;Betz,B.;Hoyer,R.;Grunwaldt,J.-D.TuningtheStructureofPlatinumParticlesonCeriaInSituforEnhancingtheCatalyticPerformanceofExhaustGasCatalysts.*Angew.Chem.,Int.Ed.***2017**,*56*,13078–13082,DOI:10.1002/anie.201707842

23. **23**

Gänzler,A.M.;Casapu,M.;Maurer,F.;Störmer,H.;Gerthsen,D.;Ferré,G.;Vernoux,P.;Bornmann,B.;Frahm,R.;Murzin,V.;Nachtegaal,M.;Votsmeier,M.;Grunwaldt,J.-D.TuningthePt/CeO_2InterfacebyinSituVariationofthePtParticleSize.*ACSCatal.***2018**,*8*,4800–4811,DOI:10.1021/acscatal.8b00330

24. **24**
Nie,L.;Mei,D.;Xiong,H.;Peng,B.;Ren,Z.;Hernandez,X.I.P.;DeLaRiva,A.;Wang,M.;Engelhard,M.H.;Kovarik,L.;Datye,A.K.;Wang,Y.ActivationofSurfaceLatticeOxygeninSingle-AtomPt/CeO_2forLow-TemperatureCOOxidation.*Science***2017**,*358*,1419–1423,DOI:10.1126/science.aao2109

25. **25**
Xiong,H.;Lin,S.;Goetze,J.;Pletcher,P.;Guo,H.;Kovarik,L.;Artyushkova,K.;Weckhuysen,B.M.;Datye,A.K.ThermallyStableandRegenerablePlatinum-TinClustersforPropaneDehydrogenationPreparedbyAtomTrappingonCeria.*Angew.Chem.,Int.Ed.***2017**,*56*,8986–8991,DOI:10.1002/anie.201701115

26. **26**
Ferré,G.;Aouine,M.;Bosselet,F.;Burel,L.;CadeteSantosAires,F.J.;Geantet,C.;Ntais,S.;Maurer,F.;Casapu,M.;Grunwaldt,J.-D.;Epicier,T.;Loridant,S.;Vernoux,P.ExploitingtheDynamicPropertiesofPtonCeriaforLow-TemperatureCOOxidation.*Catal.Sci.Technol.***2020**,*10*,3904–3917,DOI:10.1039/D0CY00732C

27. **27**
Kunwar,D.;Zhou,S.;DeLaRiva,A.;Peterson,E.J.;Xiong,H.;Pereira-Hernández,X.I.;Purdy,S.C.;terVeen,R.;Brongersma,H.H.;Miller,J.T.;Hashiguchi,H.;Kovarik,L.;Lin,S.;Guo,H.;Wang,Y.;Datye,A.K.StabilizingHighMetalLoadingsofThermallyStablePlatinumSingleAtomsonanIndustrialCatalystSupport.*ACSCatal.***2019**,*9*,3978–3990,DOI:10.1021/acscatal.8b04885

28. **28**
Zhou,J.;Baddorf,A.P.;Mullins,D.R.;Overbury,S.H.GrowthandCharacterizationofRhandPdNanoparticlesonOxidizedandReducedCeO_x(111)ThinFilmsbyScanningTunnelingMicroscopy.*J.Phys.Chem.C***2008**,*112*,9336–9345,DOI:10.1021/jp711198c

29. **29**
Lu,J.-L.;Gao,H.-J.;Shaikhutdinov,S.;Freund,H.-J.MorphologyandDefectStructureoftheCeO$_2$(111)FilmsGrownonRu(0001)asStudiedbyScanningTunnelingMicroscopy.*Surf.Sci.***2006**,*600*,5004–5010,DOI:10.1016/j.susc.2006.08.023

30. **30**
Lykhach,Y.;Kozlov,S.M.;Skála,T.;Tovt,A.;Stetsovych,V.;Tsud,N.;Dvořák,F.;Johánek,V.;Neitzel,A.;Mysliveček,J.;Fabris,S.;Matolín,V.;Neyman,K.M.;Libuda,J.CountingElectronsonSupportedNanoparticles.*Nat.Mater.***2016**,*15*,284–288,DOI:10.1038/nmat4500

31. **31**
Dvořák,F.;FarnesiCamellone,M.;Tovt,A.;Tran,N.;Negreiros,F.R.;Vorokhta,M.;Skála,T.;Matolínová,I.;Mysliveček,J.;Matolín,V.;Fabris,S.CreatingSingle-AtomPt-

CeriaCatalystsbySurfaceStepDecoration.*Nat.Commun.***2016**,*7*,10801DOI:10.1038/ncomms10801

32. **32**
Tovt,A.;Bagolini,L.;Dvořák,F.;Tran,N.-D.;Vorokhta,M.;Beranová,K.;Johánek,V.;FarnesiCamellone,M.;Skála,T.;Matolínová,I.;Mysliveček,J.;Fabris,S.;Matolín,V.UltimateDispersionofMetallicandIonicPlatinumonCeria.*J.Mater.Chem.A***2019**,*7*,13019–13028,DOI:10.1039/C9TA00823C

33. **33**
Bruix,A.;Lykhach,Y.;Matolínová,I.;Neitzel,A.;Skála,T.;Tsud,N.;Vorokhta,M.;Stetsovych,V.;Ševčíková,K.;Mysliveček,J.;Fiala,R.;Václavů,M.;Prince,K.C.;Bruyère,S.;Potin,V.;Illas,F.;Matolín,V.;Libuda,J.;Neyman,K.M.MaximumNoble-MetalEfficiencyinCatalyticMaterials:AtomicallyDispersedSurfacePlatinum.*Angew.Chem.,Int.Ed.***2014**,*53*,10525–10530,DOI:10.1002/anie.201402342

34. **34**
Hatanaka,M.;Takahashi,N.;Takahashi,N.;Tanabe,T.;Nagai,Y.;Suda,A.;Shinjoh,H.ReversibleChangesinthePtOxidationStateandNanostructureonaCeria-BasedSupportedPt.*J.Catal.***2009**,*266*,182–190,DOI:10.1016/j.jcat.2009.06.005

35. **35**
Shinjoh,H.;Hatanaka,M.;Nagai,Y.;Tanabe,T.;Takahashi,N.;Yoshida,T.;Miyake,Y.SuppressionofNobleMetalSinteringBasedontheSupportAnchoringEffectandItsApplicationinAutomotiveThree-WayCatalysis.*Top.Catal.***2009**,*52*,1967–1971,DOI:10.1007/s11244-009-9371-5

36. **36**
Lykhach,Y.;Johánek,V.;Aleksandrov,H.A.;Kozlov,S.M.;Happel,M.;Skála,T.;Petkov,P.S.;Tsud,N.;Vayssilov,G.N.;Prince,K.C.;Neyman,K.M.;Matolín,V.;Libuda,J.WaterChemistryonModelCeriaandPt/CeriaCatalysts.*J.Phys.Chem.C***2012**,*116*,12103–12113,DOI:10.1021/jp302229x

37. **37**
Matolín,V.;Matolínová,I.;Dvořák,F.;Johánek,V.;Mysliveček,J.;Prince,K.C.;Skála,T.;Stetsovych,O.;Tsud,N.;Václavů,M.;Šmíd,B.WaterInteractionwithCeO_2(111)/Cu(111)ModelCatalystSurface.*Catal.Today***2012**,*181*,124–132,DOI:10.1016/j.cattod.2011.05.032

38. **38**
Plessow,P.N.;Abild-Pedersen,F.SinteringofPtNanoparticlesviaVolatilePtO_2:SimulationandComparisonwithExperiments.*ACSCatal.***2016**,*6*,7098–7108,DOI:10.1021/acscatal.6b01646

39. **39**
Wang,X.;vanBokhoven,J.A.;Palagin,D.OstwaldRipeningversusSingleAtomTrapping:TowardsUnderstandingPlatinumParticleSintering.*Phys.Chem.Chem.Phys.***2017**,*19*,30513–30519,DOI:10.1039/C7CP05887J

40. **40**

Newton,M.A.;Belver-Coldeira,C.;Martínez-Arias,A.;Fernández-García,M.DynamicinSituObservationofRapidSizeandShapeChangeofSupportedPdNanoparticlesduringCO/NOCycling.*Nat.Mater.***2007**,*6*,528–532,DOI:10.1038/nmat1924

41. **41**
Bruix,A.;Neyman,K.M.;Illas,F.Adsorption,OxidationState,andDiffusionofPtAtomsontheCeO$_2$(111)Surface.*J.Phys.Chem.C***2010**,*114*,14202–14207,DOI:10.1021/jp104490k

42. **42**
Hlawacek,G.;Puschnig,P.;Frank,P.;Winkler,A.;Ambrosch-Draxl,C.;Teichert,C.CharacterizationofStep-EdgeBarriersinOrganicThin-FilmGrowth.*Science***2008**,*321*,108–111,DOI:10.1126/science.1159455

43. **43**
Kalff,M.;Šmilauer,P.;Comsa,G.;Michely,T.NoCoarseninginPt(111)Homoepitaxy.*Surf.Sci.***1999**,*426*,L447–L453,DOI:10.1016/S0039-6028(99)00351-9

44. **44**
Wan,Q.;Wei,F.;Wang,Y.;Wang,F.;Zhou,L.;Lin,S.;Xie,D.;Guo,H.SingleAtomDetachmentfromCuClusters,andDiffusionandTrappingonCeO$_2$(111):ImplicationsinOstwaldRipeningandAtomicRedispersion.*Nanoscale***2018**,*10*,17893–17901,DOI:10.1039/C8NR06232C

45. **45**
Tran,N.-D.;FarnesiCamellone,M.;Fabris,S.ProbingtheReactivityofPt/CeriaNanocatalyststowardMethanolOxidation:FromIonicSingle-AtomSitestoMetallicNanoparticles.*J.Phys.Chem.C***2018**,*122*,17917–17927,DOI:10.1021/acs.jpcc.8b05735

46. **46**
Kozlov,S.M.;Viñes,F.;Nilius,N.;Shaikhutdinov,S.;Neyman,K.M.AbsoluteSurfaceStepEnergies:AccurateTheoreticalMethodsAppliedtoCeriaNanoislands.*J.Phys.Chem.Lett.***2012**,*3*,1956–1961,DOI:10.1021/jz3006942

47. **47**
Ghosh,P.;FarnesiCamellone,M.;Fabris,S.FluxionalityofAuClustersatCeriaSurfacesduringCOOxidation:RelationshipsamongReactivity,Size,Cohesion,andSurfaceDefectsfromDFTSimulations.*J.Phys.Chem.Lett.***2013**,*4*,2256–2263,DOI:10.1021/jz4009079

48. **48**
Wang,Y.-G.;Mei,D.;Glezakou,V.-A.;Li,J.;Rousseau,R.DynamicFormationofSingle-AtomCatalyticActiveSitesonCeria-SupportedGoldNanoparticles.*Nat.Commun.***2015**,*6*,6511DOI:10.1038/ncomms7511

49. **49**
Bruix,A.;Rodriguez,J.A.;Ramírez,P.J.;Senanayake,S.D.;Evans,J.;Park,J.B.;Stacchiola,D.;Liu,P.;Hrbek,J.;Illas,F.ANewTypeofStrongMetal-SupportInteractionandtheProductionofH$_2$throughtheTransformationofWateronPt/CeO$_2$(111)a

ndPt/CeO_x/TiO_2(110)Catalysts.*J.Am.Chem.Soc.***2012**,*134*,8968–8974,DOI:10.1021/ja302070k

50. **50**
Ratsch,C.;Zangwill,A.;Šmilauer,P.;Vvedensky,D.D.SaturationandScalingofEpitaxialIslandDensities.*Phys.Rev.Lett.***1994**,*72*,3194–3197,DOI:10.1103/PhysRevLett.72.3194

51. **51**
Evans,J.W.;Thiel,P.A.;Bartelt,M.C.MorphologicalEvolutionduringEpitaxialThinFilmGrowth:Formationof2DIslandsand3DMounds.*Surf.Sci.Rep.***2006**,*61*,1–128,DOI:10.1016/j.surfrep.2005.08.004

52. **52**
Singh,N.;Campbell,C.T.ASimpleBond-AdditivityModelExplainsLargeDecreasesinHeatsofAdsorptioninSolventsVersusGasPhase:ACaseStudywithPhenolonPt(111)inWater.*ACSCatal.***2019**,*9*,8116–8127,DOI:10.1021/acscatal.9b01870

53. **53**
Petersen,M.;Zangwill,A.;Ratsch,C.HomoepitaxialOstwaldRipening.*Surf.Sci.***2003**,*536*,55–60,DOI:10.1016/S0039-6028(03)00580-6

54. **54**
Li,L.;Plessow,P.N.;Rieger,M.;Sauer,S.;Sánchez-Carrera,R.S.;Schaefer,A.;Abild-Pedersen,F.ModelingtheMigrationofPlatinumNanoparticlesonSurfacesUsingaKineticMonteCarloApproach.*J.Phys.Chem.C***2017**,*121*,4261–4269,DOI:10.1021/acs.jpcc.6b11549

55. **55**
Mysliveček,J.;Schelling,C.;Schäffler,F.;Springholz,G.;Šmilauer,P.;Krug,J.;Voigtländer,B.OntheMicroscopicOriginoftheKineticStepBunchingInstabilityonVicinalSi(001).*Surf.Sci.***2002**,*520*,193–206,DOI:10.1016/S0039-6028(02)02273-2

56. **56**
Cherepanov,V.;Filimonov,S.;Mysliveček,J.;Voigtländer,B.ScalingofSubmonolayerIslandSizesinSurfactant-MediatedEpitaxyofSemiconductors.*Phys.Rev.B***2004**,*70*,085401DOI:10.1103/PhysRevB.70.085401

57. **57**
Lai,K.C.;Han,Y.;Spurgeon,P.;Huang,W.;Thiel,P.A.;Liu,D.-J.;Evans,J.W.Reshaping,Intermixing,andCoarseningforMetallicNanocrystals:NonequilibriumStatisticalMechanicalandCoarse-GrainedModeling.*Chem.Rev.***2019**,*119*,6670–6768,DOI:10.1021/acs.chemrev.8b00582

58. **58**
Wettergren,K.;Schweinberger,F.F.;Deiana,D.;Ridge,C.J.;Crampton,A.S.;Rötzer,M.D.;Hansen,T.W.;Zhdanov,V.P.;Heiz,U.;Langhammer,C.HighSinteringResistanceofSize-

SelectedPlatinumClusterCatalystsbySuppressedOstwaldRipening.*NanoLett.***2014**,*14*,5803–5809,DOI:10.1021/nl502686u

59. **59**
Jeong,H.;Kwon,O.;Kim,B.-S.;Bae,J.;Shin,S.;Kim,H.-E.;Kim,J.;Lee,H.HighlyDurableMetalEnsembleCatalystswithFullDispersionforAutomotiveApplicationsbeyondSingle-AtomCatalysts.*Nat.Catal.***2020**,*3*,368–375,DOI:10.1038/s41929-020-0427-z

60. **60**
Dai,Y.;Lu,P.;Cao,Z.;Campbell,C.T.;Xia,Y.ThePhysicalChemistryandMaterialsSciencebehindSinter-ResistantCatalysts.*Chem.Soc.Rev.***2018**,*47*,4314–4331,DOI:10.1039/C7CS00650K

61. **61**
Gandhi,H.S.;Graham,G.W.;McCabe,R.W.AutomotiveExhaustCatalysis.*J.Catal.***2003**,*216*,433–442,DOI:10.1016/S0021-9517(02)00067-2

62. **62**
Iglesias-Juez,A.;Martínez-Arias,A.;Newton,M.A.;Fiddy,S.G.;Fernández-García,M.RedoxBehaviourofPd-BasedTWCsunderDynamicConditions:AnalysisUsingDispersiveXASandMassSpectrometry.*Chem.Commun.***2005**,4092,DOI:10.1039/b502798e

63. **63**
Sayle,T.X.T.;Cantoni,M.;Bhatta,U.M.;Parker,S.C.;Hall,S.R.;Möbus,G.;Molinari,M.;Reid,D.;Seal,S.;Sayle,D.C.StrainandArchitecture-TunedReactivityinCeriaNanostructures;EnhancedCatalyticOxidationofCOtoCO_2.*Chem.Mater.***2012**,*24*,1811–1821,DOI:10.1021/cm3003436

64. **64**
Sayle,T.X.T.;Caddeo,F.;Zhang,X.;Sakthivel,T.;Das,S.;Seal,S.;Ptasinska,S.;Sayle,D.C.Structure–ActivityMapofCeriaNanoparticles,Nanocubes,andMesoporousArchitectures.*Chem.Mater.***2016**,*28*,7287–7295,DOI:10.1021/acs.chemmater.6b02536

65. **65**
Pushkarev,V.V.;Kovalchuk,V.I.;D'Itri,J.L.ProbingDefectSitesontheCeO$_2$SurfacewithDioxygen.*J.Phys.Chem.B***2004**,*108*,5341–5348,DOI:10.1021/jp0311254

66. **66**
Wu,Z.;Li,M.;Howe,J.;Meyer,H.M.;Overbury,S.H.ProbingDefectSitesonCeO$_2$NanocrystalswithWell-DefinedSurfacePlanesbyRamanSpectroscopyandO$_2$Adsorption.*Langmuir***2010**,*26*,16595–16606,DOI:10.1021/la101723w

67. **67**
Kullgren,J.;Hermansson,K.;Broqvist,P.SuperchargedLow-TemperatureOxygenStorageCapacityofCeriaattheNanoscale.*J.Phys.Chem.Lett.***2013**,*4*,604–608,DOI:10.1021/jz3020524

68. **68**
Leistner,K.;GonzalezBraga,C.;Kumar,A.;Kamasamudram,K.;Olsson,L.VolatilisationandSubsequentDepositionofPlatinumOxidesfromDieselOxidationCatalysts.*Appl.Catal.,B***2019**,*241*,338–350,DOI:10.1016/j.apcatb.2018.09.022

69. **69**
Kozlov,S.M.;Neyman,K.M.OVacanciesonStepsontheCeO$_2$(111)Surface.*Phys.Chem.Chem.Phys.***2014**,*16*,7823,DOI:10.1039/c4cp00136b

70. **70**
TabibZadehAdibi,P.;Mazzotta,F.;Antosiewicz,T.J.;Skoglundh,M.;Grönbeck,H.;Langhammer,C.InSituPlasmonicSensingofPlatinumModelCatalystSinteringonDifferentOxideSupportsandinO$_2$andNO$_2$AtmospthereswithDifferentConcentrations.*ACSCatal.***2015**,*5*,426–432,DOI:10.1021/cs5015173

71. **71**
Ouyang,R.;Liu,J.;Li,W.AtomisticTheoryofOstwaldRipeningandDisintegrationofSupportedMetalParticlesunderReactionConditions.*J.Am.Chem.Soc.***2013**,*135*,1760–1771,DOI:10.1021/ja3087054

72. **72**
Porsgaard,S.;Merte,L.R.;Ono,L.K.;Behafarid,F.;Matos,J.;Helveg,S.;Salmeron,M.;RoldanCuenya,B.;Besenbacher,F.StabilityofPlatinumNanoparticlesSupportedonSiO$_2$/Si(111):AHigh-PressureX-RayPhotoelectronSpectroscopyStudy.*ACSNano***2012**,*6*,10743–10749,DOI:10.1021/nn3040167

73. **73**
Perdew,J.P.J.;Burke,K.;Ernzerhof,M.GeneralizedGradientApproximationMadeSimple.*Phys.Rev.Lett.***1996**,*77*,3865–3868,DOI:10.1103/PhysRevLett.77.3865

74. **74**
Vanderbilt,D.SoftSelf-ConsistentPseudopotentialsinaGeneralizedEigenvalueFormalism.*Phys.Rev.B***1990**,*41*,7892–7895,DOI:10.1103/PhysRevB.41.7892

75. **75**
Cococcioni,M.;deGironcoli,S.LinearResponseApproachtotheCalculationoftheEffectiveInteractionParametersintheLDA+UMethod.*Phys.Rev.B***2005**,*71*,035105DOI:10.1103/PhysRevB.71.035105

76. **76**
Fabris,S.;deGironcoli,S.;Baroni,S.;Vicario,G.;Balducci,G.TamingMultipleValencywithDensityFunctionals:ACaseStudyofDefectiveCeria.*Phys.Rev.B***2005**,*71*,041102DOI:10.1103/PhysRevB.71.041102

77. **77**
Giannozzi,P.;Baroni,S.;Bonini,N.;Calandra,M.;Car,R.;Cavazzoni,C.;Ceresoli,D.;Chiarotti,G.L.;Cococcioni,M.;Dabo,I.;DalCorso,A.;deGironcoli,S.;Fabris,S.;Fratesi,G.;Gebauer,R.;Gerstmann,U.;Go

ugoussis,C.;Kokalj,A.;Lazzeri,M.;Martin-Samos,L.;Marzari,N.;Mauri,F.;Mazzarello,R.;Paolini,S.;Pasquarello,A.;Paulatto,L.;Sbraccia,C.;Scandolo,S.;Sclauzero,G.;Seitsonen,A.P.;Smogunov,A.;Umari,P.;Wentzcovitch,R.M.QUANTUMESPRESSO:AModularandOpen-SourceSoftwareProjectforQuantumSimulationsofMaterials.*J.Phys.:Condens.Matter***2009**,*21*,395502DOI:10.1088/0953-8984/21/39/395502

78. **78**
Bortz,A.B.;Kalos,M.H.;Lebowitz,J.L.ANewAlgorithmforMonteCarloSimulationofIsingSpinSystems.*J.Comput.Phys.***1975**,*17*,10–18,DOI:10.1016/0021-9991(75)90060-1

79. **79**
Ratsch,C.;Šmilauer,P.;Zangwill,A.;Vvedensky,D.D.SubmonolayerEpitaxywithoutaCriticalNucleus.*Surf.Sci.***1995**,*329*,L599–L604,DOI:10.1016/0039-6028(95)00353-3